Electronic Supplementary Material (ESI) for Environmental Science: Nano.

Supplementary Information

Nitrogen-rich porous polymeric carbon nitride with enhanced photocatalytic activity for synergistic removal of organic and heavy metal pollutants

Xiangyang Li[a], Keyan Li [a,*], Jun Du[a], Mengjiao Pei[a], Chunshan Song[a,b], Xinwen Guo[a,*]

[a]State Key Laboratory of Fine Chemicals, PSU-DUT Joint Center for Energy Research, School of Chemical Engineering, Dalian University of Technology, Dalian 116024, China.

[b]Department of Chemistry, Faculty of Science, The Chinese University of Hong Kong, Shatin, Hong Kong 999077, China

*Corresponding Author. E-mail address: keyanli@dlut.edu.cn; guoxw@dlut.edu.cn.

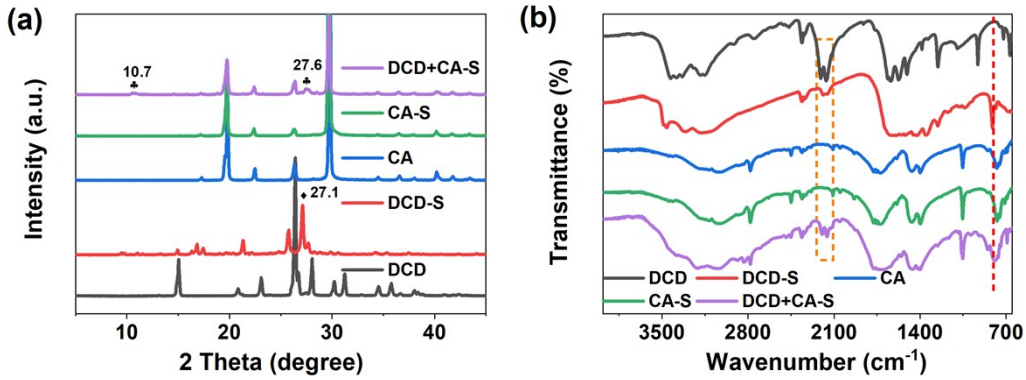

Fig. S1. XRD patterns (a) and FT-IR spectra (b) of DCD, DCD-S, CA, CA-S and DCD+CA-S.

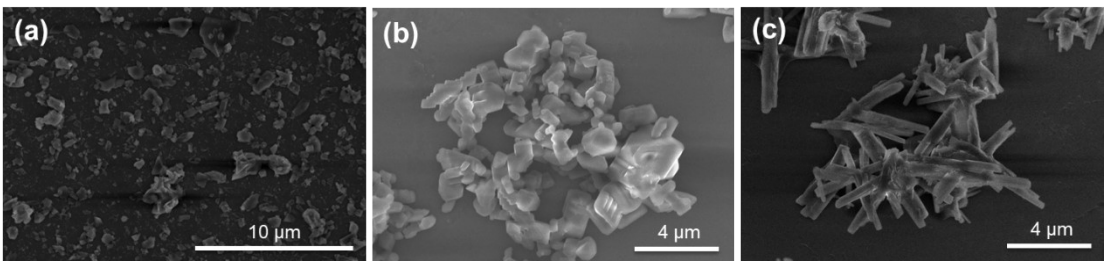

Fig. S2. SEM images of DCD-S (a), CA-S (b) and DCD+CA-S (c).

The effect of solvothermal process

To understand the effect of the solvothermal process on the samples, we first studied the XRD patterns of solvothermally treated DCD, CA and DCD+CA (named as DCD-S, CA-S and DCD+CA-S, respectively). From Fig. S1a, the diffraction peaks of DCD-S change obviously compared to DCD. The diffraction peak at 27.1° belongs to the stacking of graphite-like layers,[1,2] indicating that DCD is totally converted to polymer intermediate after solvothermal process. By contrast, the structure of CA-S has no obvious change compared to CA, indicating that solvothermal treatment has little effect on CA. The XRD pattern of CA+DCD-S is similar to that of CA. However, the diffraction peaks at 10.7° and 27.6° can be clearly observed, which can be attributed to (100) and (002) planes of CN,[3] indicating that a part of CA polymerizes with DCD to form CN framework during the solvothermal process and there are still some CA remaining in CA+DCD-S. The chemical structure of the intermediate was further studied by FT-IR spectra (Fig. S1b). The spectrum of DCD-S changes significantly compared to DCD. A breathing vibration peak belonging to the heptazine structural unit is found at 810 cm^{-1}, demonstrating that DCD forms a polymer containing the heptazine structural units.[4] The weakening of the cyano signal in 2100–2200 cm^{-1} also demonstrates the initial polymerization of DCD during the solvothermal process.[5] The FT-IR spectrum of CA-S is basically unchanged compared to CA, consistent with the XRD patterns. The spectrum of DCD+CA-S is similar to that of CA, but also exhibits a stretching vibration peak of the heptazine structural unit at 810 cm^{-1}. Fig. S2 shows the SEM images of DCD-S, CA-S and DCCN-S. It can be clearly seen that DCD-S and CA-S have irregular blocky morphology (Fig. S2a and b). However, DCD+CA-S shows rodlike morphology (Fig. S2c). The above results indicate that the solvothermal process is conducive to the initial polymerization of DCD and the generation of rich defect sites. The addition of CA promotes the formation of CN framework. Simultaneously, the unreacted CA may be uniformly distributed in the polymer intermediate through hydrogen bonding, which acts as a porogen during the calcination process.

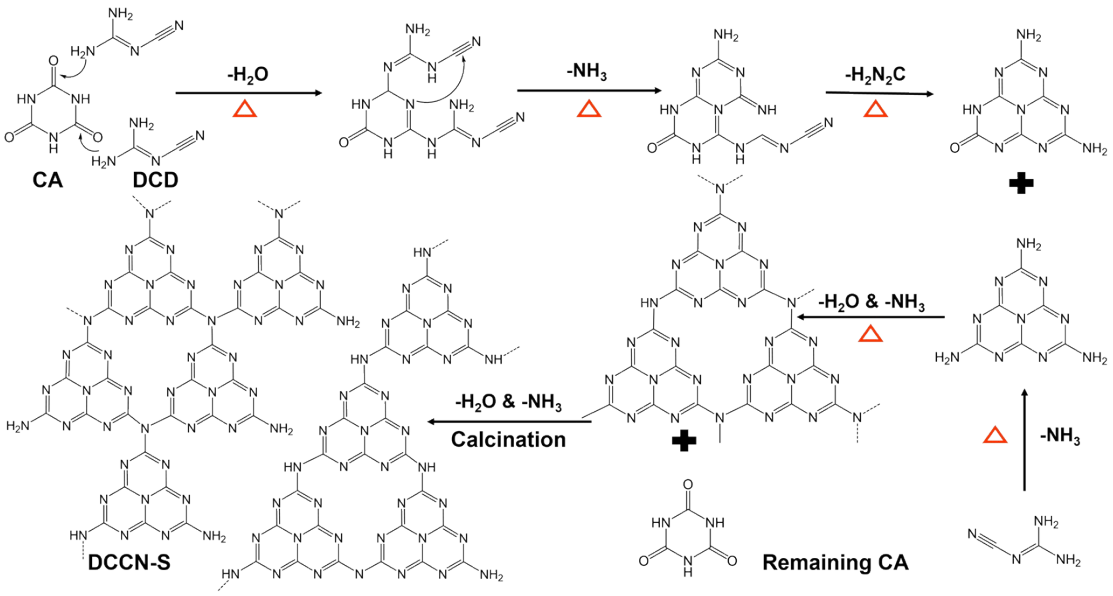

Scheme S1. Possible copolymerization process of DCCN-S.

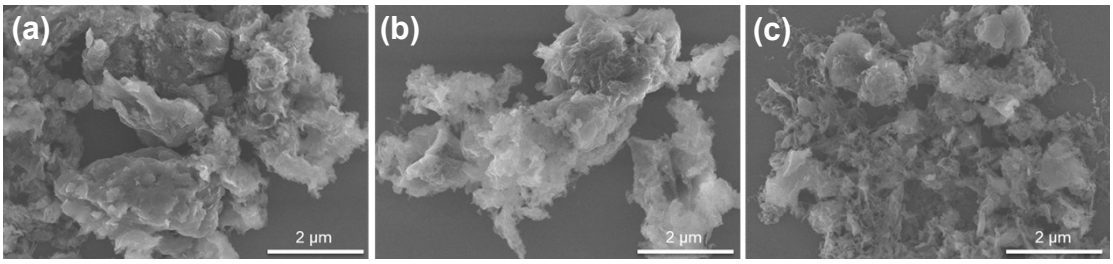

Fig. S3. SEM images of DCCN-S with different ratios of CA to DCD: (a) 1 g of DCD and 0.5 g of CA, (b) 1 g of DCD and 1 g of CA and (c) 1 g of DCD and 3 g of CA.

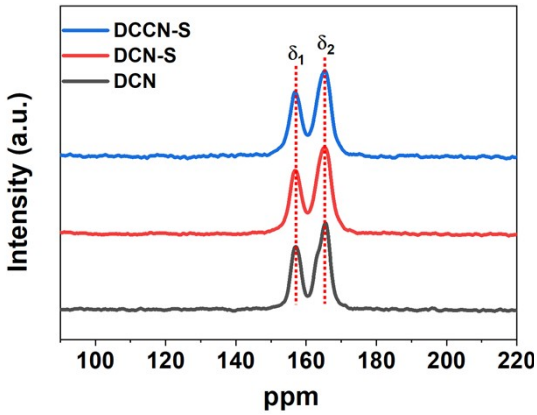

Fig. S4. ^{13}C CPMAS NMR of DCN, DCN-S and DCCN-S.

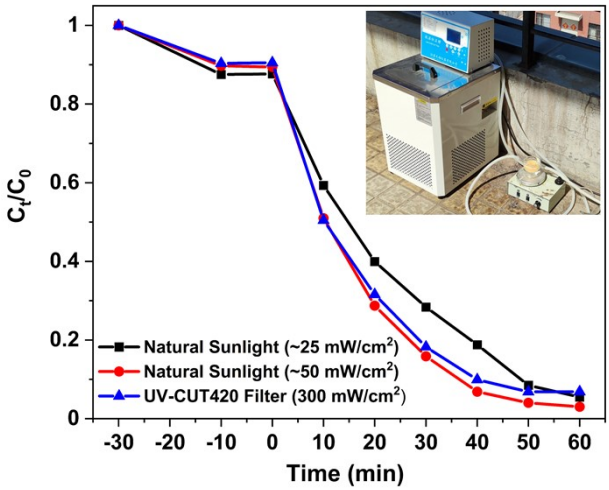

Fig. S5. Removal rates of LEV over DCCN-S under natural sunlight (10:30 to 11:30 am, April, Dalian) and visible light using Xe lamp with a UV-CUT420 filter.

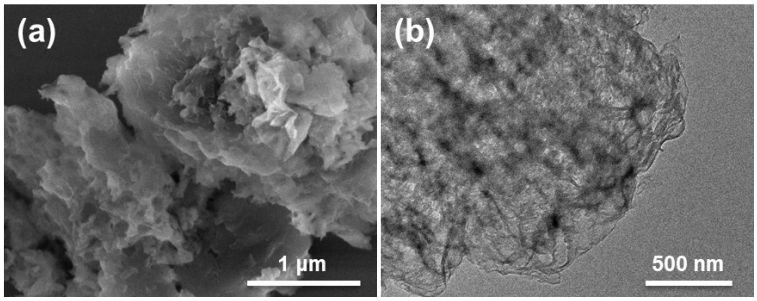

Fig. S6. SEM (a) and TEM (b) images of DCCN-S after six photocatalytic cycles.

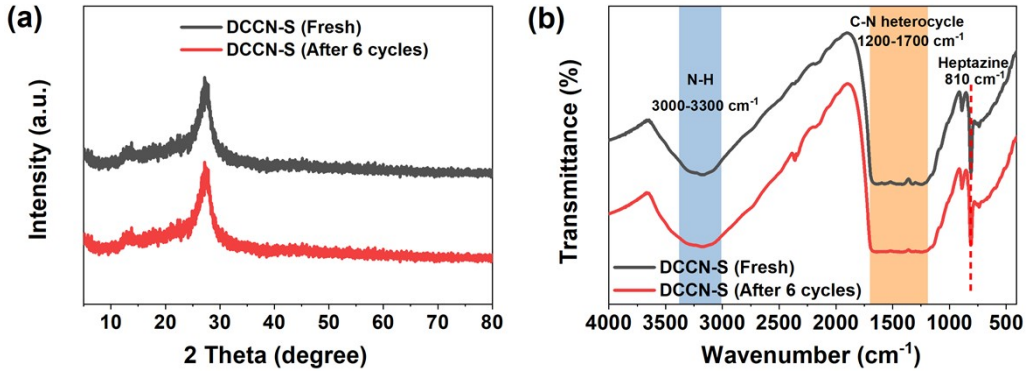

Fig. S7. XRD patterns (a) and FT-IR spectra (b) of fresh DCCN-S and DCCN-S after six photocatalytic cycles.

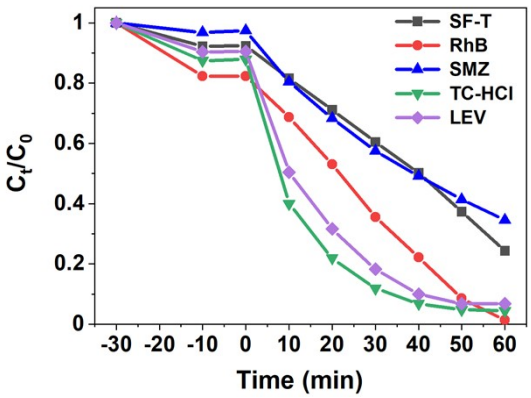

Fig. S8. Removal curves of various organic pollutants over DCCN-S under visible light irradiation.

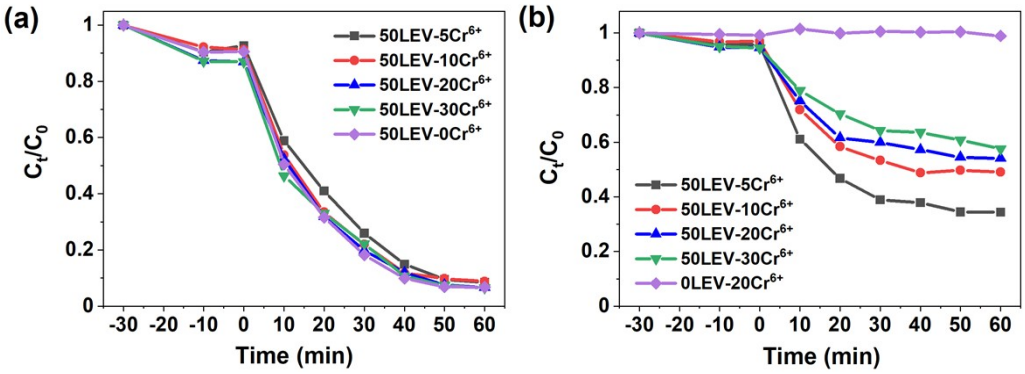

Fig. S9. Removal curves of simultaneous photocatalytic oxidation of LEV (a) and reduction of Cr(VI) (b) over DCCN-S under visible light irradiation.

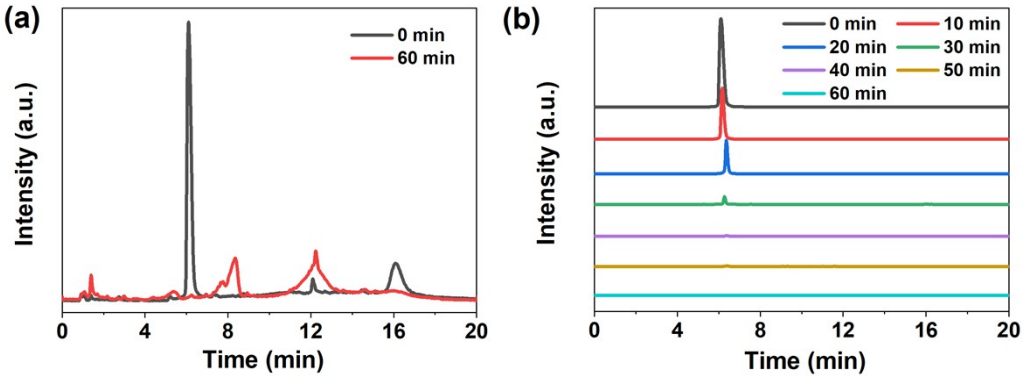

Fig. S10. High performance liquid chromatogram spectra of LEV aqueous solution at 0 min and 60 min of visible light irradiation in the presence of DCCN-S (a), the change of peak at m/z = 362.4 with time in the MS spectra (b).

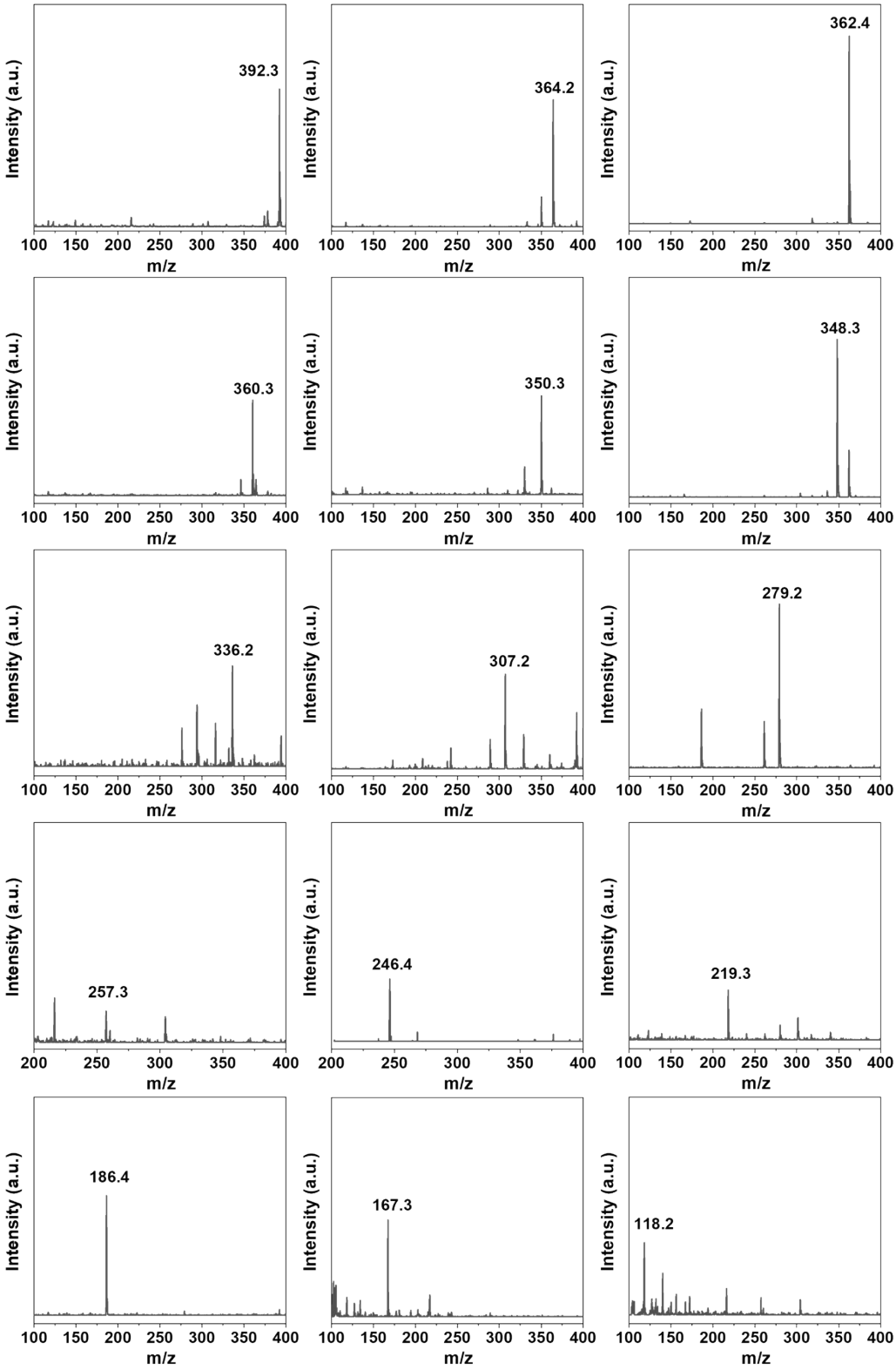

Fig. S11. MS spectra of the intermediates in the process of LEV degradation.

Table S1. BET specific surface (S_{BET}) and pore volume (V_P) of the samples.

Sample	S_{BET} ($m^2\ g^{-1}$)	V_P ($cm^3\ g^{-1}$)
DCN	18.6	0.20
DCN-S	12.7	0.18
DCCN-S	52.0	0.46

Table S2. Peak areas obtained by N 1s XPS spectra.

Sample	N_{2C}	N_{3C}	C-NH_x	N_{2C}/N_{3C}	N_{2C}/C-NH_x
DCN	27546.2	4600.4	3558.5	6.0	7.7
DCN-S	26560.0	4118.7	3698.7	6.4	7.2
DCCN-S	34569.6	5235.4	4983.0	6.6	6.9

Table S3. The results of element analysis.

Sample	N (%)	C (%)	H (%)	C/N
DCN	52.83	35.14	1.74	0.665
DCN-S	53.73	33.93	2.20	0.631
DCCN-S	54.49	34.16	2.17	0.627

Table S4. Comparison of LEV photodegradation performance of DCCN-S with those of other photocatalysts reported in the literature.

Photocatalyst	LEV concentration (mg L^{-1})	Catalyst dosage (g L^{-1})	Light source	Time (min)	Removal rate (%)	Ref.
$MoS_2/Ag_2Mo_2O_7$	5	1	150W XL (Solar light)	90	97	6
CN/BiOBr	10	1	300W XL (λ>420 nm)	50	100	7
$Bi@Bi_5O_7I$/rGO	20	-	300W XL (λ>420 nm)	60	87.7	8
$Ag/Ag_2S/Bi_2MoO_6$	20	0.3	300W XL (λ>400 nm)	120	87.3	9
BiOI/g-C_3N_4/graphene	20	0.25	300W XL (λ>420 nm)	180	63	10
Ag_2CO_3/CeO_2/AgBr	10	0.5	300W XL (λ>420 nm)	40	87.63	11
PDI/g-C_3N_4	20	1	300W XL (λ>420 nm)	30	90	12
Au/Ni_2P/g-C_3N_4	10	1	300W XL (λ>400 nm)	120	88.23	13
$SrTiO_3$/(Ag/Fe_3O_4)/g-C_3N_4	10	0.2	500W XL (λ>420 nm)	90	98.2	14
K-g-C_3N_4	10	1	300W XL (λ>420 nm)	60	100	15
Cu/O-g-C_3N_4	15	1	300W XL (λ>420 nm)	60	98.2	16
CQDs@In_2S_3/SWNTs	15	0.8	350W XL (λ>400 nm)	60	80	17
$ZnFe_2O_4$/NCDs/Ag_2CO_3	10	0.6	300W XL (λ>420 nm)	90	88.75	18
$(BiOBr)_x(Bi_7O_9I_3)_{1-x}$	50	1	400 W halogen bulb (Solar light)	120	95.4	19
DCCN-S	50	0.5	300W XL (λ>420 nm)	60	93.5	This work

Table S5 Detailed ECOSAR values concerning LEV and the degradation intermediates.

INTERMEDIATES	Fish		Daphnia		Green Algae	
	96 h LC50	ChV	48 h LC50	ChV	96 h EC50	ChV
LEV (M/Z=362)	2.81×10^{5}	2.16×10^{4}	1.30×10^{5}	7.21×10^{3}	4.18×10^{4}	6.97×10^{3}
Route I						
M/Z=392	6.55×10^{5}	4.84×10^{4}	2.93×10^{5}	1.48×10^{4}	8.19×10^{4}	1.26×10^{4}
M/Z=364	1.54×10^{5}	1.22×10^{4}	7.33×10^{4}	4.38×10^{3}	2.64×10^{4}	4.67×10^{3}
M/Z=364	4.26×10^{6}	2.83×10^{5}	1.74×10^{6}	6.89×10^{4}	3.39×10^{5}	4.32×10^{4}
M/Z=336	9.91×10^{5}	7.10×10^{4}	4.33×10^{5}	2.03×10^{4}	1.09×10^{5}	1.59×10^{4}
M/Z=307	2.57×10^{4}	2.22×10^{3}	1.31×10^{4}	9.60×10^{2}	6.37×10^{3}	1.32×10^{3}
M/Z=279	2.62×10^{4}	2.25×10^{3}	1.33×10^{4}	9.60×10^{2}	6.33×10^{3}	1.30×10^{3}
M/Z=246	8.32×10^{4}	6.68×10^{3}	4.00×10^{4}	2.46×10^{3}	1.50×10^{4}	2.72×10^{3}
M/Z=167	8.58×10^{6}	5.29×10^{5}	3.30×10^{6}	1.09×10^{5}	4.89×10^{5}	5.37×10^{4}
Route II						
M/Z=348	4.18×10^{5}	3.14×10^{4}	1.90×10^{5}	9.96×10^{3}	5.63×10^{4}	8.98×10^{3}
M/Z=364	2.84×10^{4}	2.47×10^{3}	1.46×10^{4}	1.08×10^{3}	7.17×10^{3}	1.50×10^{3}
M/Z=350	6.48×10^{4}	5.83×10^{3}	3.20×10^{4}	2.12×10^{3}	1.34×10^{4}	2.58×10^{3}
M/Z=219	4.78×10^{3}	3.93×10^{2}	2.34×10^{3}	1.52×10^{2}	9.53×10^{2}	1.80×10^{2}
M/Z=118	2.89×10^{5}	2.09×10^{4}	1.27×10^{5}	6.11×10^{3}	3.31×10^{4}	4.92×10^{3}
Route III						
M/Z=360	1.14×10^{6}	8.15×10^{4}	4.96×10^{5}	2.31×10^{4}	1.23×10^{4}	1.78×10^{4}
M/Z=392	1.23×10^{3}	1.12×10^{2}	6.58×10^{2}	54.3	3.83×10^{2}	87.7
M/Z=364	4.86×10^{3}	4.10×10^{2}	2.44×10^{3}	1.68×10^{2}	1.08×10^{3}	2.15×10^{2}
M/Z=336	7.43×10^{3}	6.89×10^{2}	4.04×10^{3}	3.48×10^{2}	2.50×10^{3}	5.94×10^{2}
M/Z=257	2.31×10^{8}	1.23×10^{7}	7.82×10^{7}	1.80×10^{6}	6.84×10^{6}	5.66×10^{5}
M/Z=186	1.22×10^{9}	5.82×10^{7}	3.77×10^{8}	6.81×10^{6}	2.29×10^{7}	1.56×10^{6}

(Unit: mg L^{-1}; LC50 represents half lethal concentration; EC50 represents half effective concentration; ChV, chronic value, represents chronic toxicity, which is defined as the geometric mean of the no observed effect concentration and the lowest observed effect concentration.)

References

1 X. Wang, K. Maeda, A. Thomas, K. Takanabe, G. Xin, J.M. Carlsson, K. Domen, M. Antonietti, A metal-free polymeric photocatalyst for hydrogen production from water under visible light, *Nat. Mater.*, 2009, **8**, 76-80.

2 Q. Yang, S. Hu, Y. Yao, X. Lin, H. Du, Y. Yuan, Engineering graphitic carbon nitride with expanded interlayer distance for boosting photocatalytic hydrogen evolution, *Chinese J. Catal.*, 2021, **42**, 217-224.

3 P. Xia, M. Antonietti, B. Zhu, T. Heil, J. Yu, S. Cao, Designing defective crystalline carbon nitride to enable selective CO_2 photoreduction in the gas phase, *Adv. Funct. Mater.*, 2019, **29**, 1900093.

4 Y. Wang, H. Wang, F. Chen, F. Cao, X. Zhao, S. Meng, Y. Cui, Facile synthesis of oxygen doped carbon nitride hollow microsphere for photocatalysis, *Appl. Catal. B: Environ.*, 2017, **206**, 417-425.

5 X. Hu, P. Lu, R. Pan, Y. Li, J. Bai, Y. He, C. Zhang, F. Jia, M. Fu, Metal-ion-assisted construction of cyano group defects in g-C_3N_4 to simultaneously degrade wastewater and produce hydrogen, *Chem. Eng. J.*, **2**021, **423**, 130278.

6 S. Adhikari, S. Mandal, D.-H. Kim, Z-scheme 2D/1D MoS_2 nanosheet-decorated $Ag_2Mo_2O_7$ microrods for efficient catalytic oxidation of levofloxacin, *Chem. Eng. J.*, 2019, **373**, 31-43.

7 B. Chen, L. Zhou, Y. Tian, J. Yu, J. Lei, L. Wang, Y. Liu, J. Zhang, Z-scheme inverse opal CN/BiOBr photocatalysts for highly efficient degradation of antibiotics, *Phys. Chem. Chem. Phys.*, 2019, **21**, 12818-12825.

8 C. Liang, C.G. Niu, L. Zhang, X.J. Wen, S.F. Yang, H. Guo, G.M. Zeng, Construction of 2D heterojunction system with enhanced photocatalytic performance: Plasmonic Bi and reduced graphene oxide co-modified Bi_5O_7I with high-speed charge transfer channels, *J. Hazard. Mater.*, 2019, **361**, 245-258.

9 S. Li, C. Wang, Y. Liu, B. Xue, W. Jiang, Y. Liu, L. Mo, X. Chen, Photocatalytic degradation of antibiotics using a novel $Ag/Ag_2S/Bi_2MoO_6$ plasmonic p-n

heterojunction photocatalyst: Mineralization activity, degradation pathways and boosted charge separation mechanism, *Chem. Eng. J.*, 2021, **415**, 128991.

10 J. Li, X. Yu, Y. Zhu, X. Fu, Y. Zhang, 3D-2D-3D BiOI/porous g-C_3N_4/graphene hydrogel composite photocatalyst with synergy of adsorption-photocatalysis in static and flow systems, *J. Alloys Compd*., 2021, **850**, 156778.

11 X.-J.Wen, C.-G. Niu, H. Guo, L. Zhang, C. Liang, G.-M. Zeng, Photocatalytic degradation of levofloxacin by ternary Ag_2CO_3/CeO_2/AgBr photocatalyst under visible-light irradiation: Degradation pathways, mineralization ability, and an accelerated interfacial charge transfer process study, *J. Catal.*, 2018, **358**, 211-223.

12 X. Wang, J. Meng, X. Yang, A. Hu, Y. Yang, Y. Guo, Fabrication of a perylene tetracarboxylic diimide-graphitic carbon nitride heterojunction photocatalyst for efficient degradation of aqueous organic pollutants, *ACS Appl. Mater. & Inter.*, 2019, **11**, 588-602.

13 Y.Q. He, F. Zhang, B. Ma, N. Xu, L. Binnah Junior, B. Yao, Q. Yang, D. Liu, Z. Ma, Remarkably enhanced visible-light photocatalytic hydrogen evolution and antibiotic degradation over g-C_3N_4 nanosheets decorated by using nickel phosphide and gold nanoparticles as cocatalysts, *Appl. Surf. Sci*., 2020, **517**, 146187.

14 A. Kumar, A. Rana, G. Sharma, M. Naushad, A.H. Al-Muhtaseb, C. Guo, A. Iglesias-Juez, F.J. Stadler, High-performance photocatalytic hydrogen production and degradation of levofloxacin by wide spectrum-responsive Ag/Fe_3O_4 bridged $SrTiO_3$/g-C_3N_4 plasmonic nanojunctions: Joint effect of Ag and Fe_3O_4, *ACS Appl. Mater. & Inter*., 2018, **10**, 40474-40490.

15 J. Lei, B. Chen, L. Zhou, N. Ding, Z. Cai, L. Wang, S.-I. In, C. Cui, Y. Zhou, Y. Liu, J.Zhang, Efficient degradation of antibiotics in different water matrices through the photocatalysis of inverse opal K-g-C_3N_4: Insights into mechanism and assessment of antibacterial activity, *Chem. Eng. J*., 2020, **400**, 125902.

16 F. Li, P. Zhu, S. Wang, X. Xu, Z. Zhou, C. Wu, One-pot construction of Cu and O co-doped porous g-C_3N_4 with enhanced photocatalytic performance towards the degradation of levofloxacin, *RSC Adv.*, 2019, **9**, 20633-20642.

17 J. Li, Y. Ma, Z. Ye, M. Zhou, H. Wang, C. Ma, D. Wang, P. Huo, Y. Yan, Fast

electron transfer and enhanced visible light photocatalytic activity using multi-dimensional components of carbon quantum dots@3D daisy-like In_2S_3/single-wall carbon nanotubes, *Appl. Catal. B: Environ*., 2017, **204**, 224-238.

18 L. Li, C.-G. Niu, H. Guo, J. Wang, M. Ruan, L. Zhang, C. Liang, H.-Y. Liu, Y.-Y. Yang, Efficient degradation of levofloxacin with magnetically separable $ZnFe_2O_4$/NCDs/Ag_2CO_3 Z-scheme heterojunction photocatalyst: Vis-NIR light response ability and mechanism insight, *Chem. Eng. J.*, 2020, **383**, 123192.

19 S.G. Fard, M. Haghighi, M. Shabani, Facile one-pot ultrasound-assisted solvothermal fabrication of ball-flowerlike nanostructured $(BiOBr)_x(Bi_7O_9I_3)_{1-x}$ solid-solution for high active photodegradation of antibiotic levofloxacin under sun-light, *Appl. Catal. B: Environ*., 2019, **248**, 320-331.